Electronic Journal of Structural Engineering

Original Article

Cite this: DOI:10.56748/ejse.26893

Received Date:25 September 2025
Accepted Date:19 March 2026

1443-9255
https://ejsei.com/ejse

Experimental Study of the Bending Behavior of Concrete Slabs Incorporating Coal Gasification Ash Slag

Kang Ma [a,b,c*], Yan Gao [a], Ziyi Mao [a], Ruoyang Wu [d]

[a] School of Civil Engineering, Hebei Province Housing Construction Projects Regeneration Technology Innovation Center， Hebei University of Science and Technology, Shijiazhuang 050018, China
[b] China Hebei Construction & Geotechnical Investigation Group Limited, Key Laboratory for Industrial Solid Waste Comprehensive Utilization of Hebei province, Shijiazhuang 050227, China
[c] Hebei Province Engineering Research Center for Harmless Synergistic Treatment and Recycling of Municipal Solid Waste. Yanshan University, Qinhuangdao 066000, China
[d] Herriman, Utah 84096, USA
*Corresponding author: luya4426@126.com

Abstract

This study investigates the flexural behavior of concrete slabs incorporating 20% coal gasification slag (CGS) as a partial cement replacement. Experimental tests were conducted on C30, C40, and C50 grade slabs, with key results demonstrating that CGS enhances the load-bearing capacity of C40 slabs by 15% and improves ductility by 22%, while the effects on C30 and C50 slabs are less significant. These findings were supported by finite element simulations in ABAQUS, which accurately reproduced the load–deflection response and failure modes. The improvement in performance is attributed to the pozzolanic reaction of CGS, where silicates and aluminates react with cement hydrates to form C-S-H gels, refining the microstructure and enhancing crack resistance. The simulations confirmed the reliability of the proposed model in predicting structural behavior. These results underscore CGS's potential as a sustainable material for concrete, offering both improved mechanical performance and environmental benefits through reduced cement consumption.

Keywords

Coal gasification slag, Flexural performance, Concrete slabs, Compressive strength, Simulation

1. Introduction

The growth of industrialization and urbanization worldwide has made Portland cement one of the greatest industrial products on the planet. It is used extensively in the construction of roads, bridges, buildings and other infrastructure. Massive emissions of carbon dioxide are widely recognized to contribute to global warming and, consequently, climate change. Environmental concerns about the adverse effects of economic development and industrialization have compelled countries to explore alternative ways and means of reducing the levels of carbon dioxide and other toxic gas emissions.

Coal gasification slag (CGS) is composed of SiO_2, Al_2O_3, CaO, Fe_2O_3 and residual carbon, and its main mineral phase is amorphous aluminosilicate mixed with quartz crystal phase minerals (Li et al. 2019; Matjie et al. 2008). Coal gasification slag is a solid residue formed by inorganic minerals in coal through different physicochemical transformations accompanied by residual carbon particles in coal in the process of incomplete combustion of coal with oxygen or oxygen-enriched air to generate CO and H_2, which can be divided into two categories: coarse slag and fine slag. Coarse slag is generated in the slag discharge of the gasifier, whereas fine slag is generated in the syngas dust removal device.

In 2022, the annual production of CGS in China will exceed 50 million tons (Guo et al. 2024), of which coal gasification coarse slag (CGCS) and coal gasification fine slag (CGFS) account for 60% - 80% and 20% - 40%, respectively (Jiang et al. 2021). Currently, the disposal of CGS is dominated by traditional stockpiles and landfills, as shown in Fig. 1(a).

CGS contains different amounts of heavy metals, which can negatively affect the environment (Zhang et al. 2024). To achieve green mining and clean use of coal resources, environmental problems such as coal mine subsidence and coal gasification slag solid waste storage need to be solved (Yang et al. 2023).

Coal gasification slag has four main uses: first, it can be used in the production of various building materials to provide alternative raw materials for the construction industry (Fu et al. 2022; Luo et al. 2021; Zeng et al. 2023); second, coal gasification slag has important applications in soil and water treatment (Xiang et al. 2023; Xiang et al. 2020); third, the residual carbon in coal gasification slag can be extracted and utilized to further improve the efficiency of resource utilization (Zhang et al. 2020; Guo et al. 2020); and finally, it can be processed into a porous material, which is widely used in filtration and adsorption (Zhang et al. 2021). These uses fully reflect the extensive potential and value of coal gasification ash in various fields.

A study by Yoshitaka et al. (2012, p.25-27) revealed that concrete with fine CGS aggregates was superior to concrete with natural aggregates in terms of compressive strength and dry shrinkage. Aineto et al. (2005, p.11-15) succeeded in producing lightweight aggregates via CGS, demonstrating its potential as new building material. A study by Pomykala (2014, p.1403-1406) incorporated CGS powder into PC-based concrete, and the results showed that the incorporation of CGS powder had less effect on the compressive and flexural strengths of the concrete, which suggests that CGS powder can be used as an additive in concrete without significantly altering the mechanical properties.

Studies have shown that different admixtures of coal gasification ash have different effects on concrete properties, especially in the application of structural materials such as concrete slabs, which exhibit complex mechanisms of action. Concrete slabs are subjected mainly to bending loads during use, as shown in Fig. 1(b), and their strength is a key factor in determining their safety and applicability; therefore, exploring the strength properties of coal gasification ash concrete slabs is highly important.

Adequate incorporation of coal gasification ash slag (usually in the range of 10% to 20%) can improve the compressive and flexural strengths of concrete slabs, reduce porosity, and thus enhance the overall durability of concrete. Although coal gasification ash slag concrete slabs have demonstrated theoretically good application prospects, some challenges in practical engineering applications remain, such as the uniform distribution of coal gasification ash slag, reaction rate control, and long-term durability.

This study investigates the effect of incorporating coal gasification ash (CGS) on the structural properties of concrete slabs of different strength grades, addressing the research gap regarding the impact of CGS on concrete at varying replacement ratios and strength levels. While previous studies have primarily focused on the general mechanical properties of CGS-modified concrete, this study aims to provide a more detailed analysis of its performance across different concrete grades (C30, C40, and C50). By establishing a strength model through experimental data and finite element simulations, the study also explores the underlying mechanisms, specifically the pozzolanic reaction of CGS, which enhances concrete durability and strength. The core contribution of this work lies in its comprehensive analysis of CGS's effect on both structural performance and environmental sustainability, providing practical data for the use of CGS in construction materials to promote a circular economy, reduce industrial waste, and enhance resource efficiency.

Fig. 1 Engineering background: (a) Ash accumulation method (b) Bending of the floor slab

2. Experimental Program

2.1 Materials

Concrete materials

The physical properties of all the components of the concrete mixtures were in accordance with Chinese standards and specifications. The concrete mixture consisted of cement, fine aggregate, coarse aggregate, coal gasification ash and water. Ordinary silicate cement PO 42.5 was used for cementitious materials, locally produced crushed stone and natural yellow sand were used for sand and gravel, local river sand was passed through IS480 sieve mesh with a 4.75 mm aperture maintained at 150 μm before use, and crushed stone with a maximum aperture of 16 mm was used as the coarse aggregate. Tap water was used for mixing and curing the concrete, and the water reducing agent used was a polycarboxylic acid high-efficiency water reducing agent produced by Kajiangsu Building Materials Co.

The chemical composition of the materials was analyzed in the preliminary stage, as shown in Table 1. The details of the materials and mixing ratios are shown in Table 2. The coal gasification slag (CGS) used in this study exhibits a fine particle size distribution (D50 ≈ 13.6 μm) and a relatively high specific surface area of approximately 329 m^2/kg, which provides favorable conditions for micro-filling and potential secondary hydration effects in the cement matrix in Fig. 2.

Table 1. Chemical properties of the different material compositions (%)

Material	SiO_2	CaO	Al_2O_3	Fe_2O_3	Others
CGS	35.34	30.62	14.60	13.23	6.21
Cement	18.22	63.92	6.7	3.38	7.78
Coal Ash	53.01	10.48	19.45	7.42	9.64

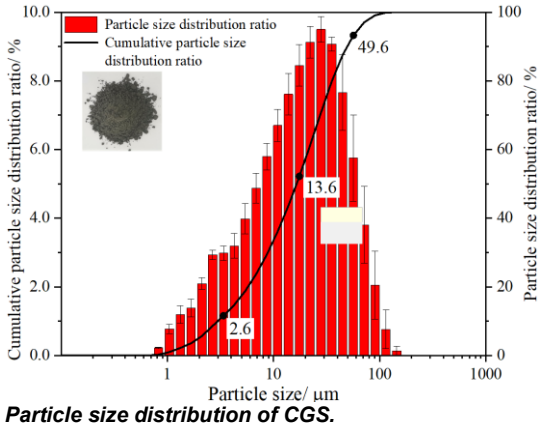

Fig. 2. Particle size distribution of CGS.

Table 2. Details of the materials and mix proportions

Material	Water (kg)	Cement (kg)	Sand (kg)	Coarse Aggregate (kg)	CGS (kg)	Water reducing agent(kg)
C40-0	14	31	64	95	0	0.31
C40-2	14	25	64	95	6.2	0.31
C30-2	14	34	66	99	6.8	0.28
C50-2	14	44	62	93	8.8	0.77

For concrete containing different admixtures of coal gasification slag, first after a series of mechanical tests, as shown in Fig. 3, to obtain the properties shown in Table 3, the material number was expressed, for example, C40-2, that is, the water–cement ratio needed to meet the standards of C40 concrete and the admixture of 20% coal gasification slag with a size of 100 mm in the cubic coal gasification slag concrete test block. It can be seen from Table 3 that the compressive strength and splitting tensile strength of concrete made of coal gasification slag instead of 20 % cement are significantly higher than those of ordinary concrete.

The uniaxial compressive stress-strain relationship of the mixture of coal gasification ash and ordinary Portland cement concrete is shown in Fig. 3. Here, the stress-strain relationships of three strength grades are presented. Generally, the stress-strain relationship of coal gasification ash and ordinary Portland cement concrete is similar. The initial rising stage of the stress-strain curve of the coal gasification ash slag concrete is larger than the slope of its ordinary Portland cement concrete counterpart, indicating that its elastic modulus is higher. SEM observations further indicate a relatively denser matrix morphology in CGS-modified concrete, which is consistent with the enhanced flexural behavior observed at the structural level in Fig. 4.

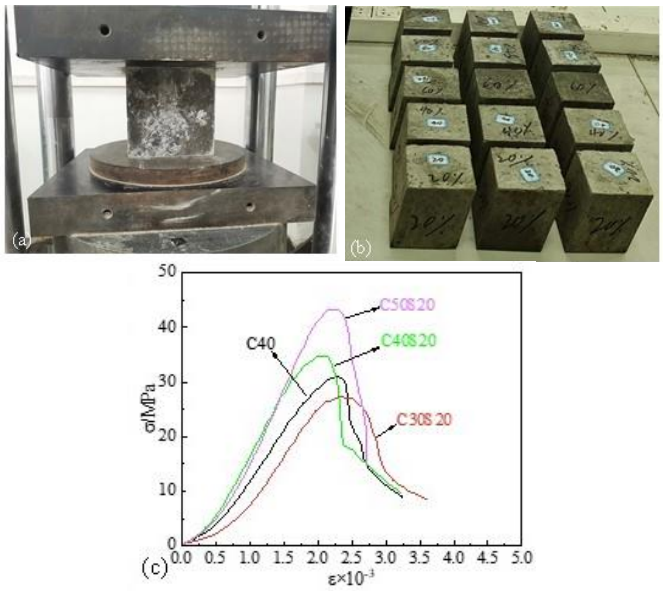

Fig. 3. Mechanics experiment (a) Cube compressive strength test (b) Test block (c) Stress–strain curve of coal gasification ash concrete

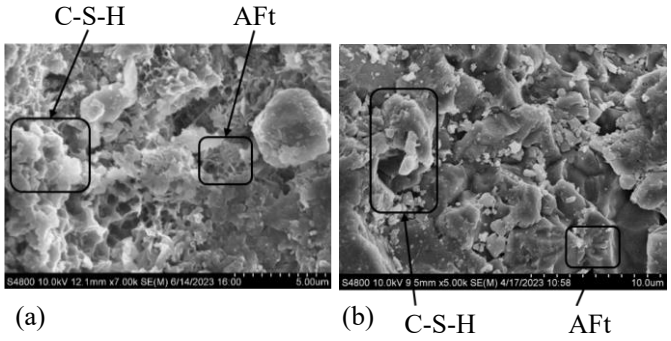

Fig. 4. SEM micrographs of CGS-modified concrete

All the samples of coal gasification ash concrete were expressed in the form of C-T-G, where "T" is the compressive strength of the concrete (30 MPa, 40 MPa and 50 MPa) and "G" is the admixture amount of coal gasification ash (the admixture amounts were 0% and 20% are 0 and 2, respectively).

Table 3. Mechanical parameters of the concrete

Material	Compressive strength (MPa)		Splitting tensile strength (MPa)	
	(1) 17 days	(2) 28 days	(1) 7 days	(2) 28 days
C40	31.9	40.7	2.0	2.5
C40+2	32.5	45.2	2.5	3.4
C30+2	24.8	34.6	2.2	2.9
C50+2	41.9	58.3	2.8	3.8

Reinforcing bars

Reinforcing steel was used to reinforce the gasified ash concrete slabs. A batch of 8 mm diameter rebars was used, and the results of direct tensile tests, including the modulus of elasticity, yield stress, yield strain, ultimate strength and ultimate strain, are shown in Table 4.

Table 4. Material properties of the steel rebar

Rebar type	d_r (mm)	E_s (GPa)	f_y (MPa)	f_u (MPa)
HRB400	8	1.64	316	390

Note: d_r is the nominal diameter of the rebar; E_s is the modulus of elasticity of the rebar; F_y is the yield stress of the rebar; ε_y is the strain under the yield stress; and f_u is the ultimate stress of the rebar.

2.2 Test models

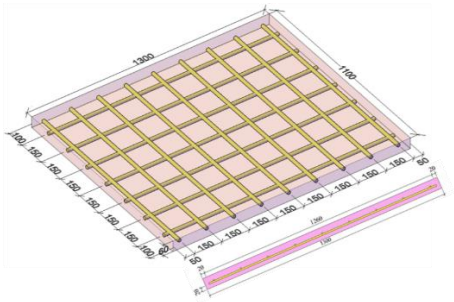

Fig. 5 Schematic of the plate

Flexural tests were carried out on four reinforced concrete slab samples. All the slab samples had the same dimensions, i.e., 1,100 mm x 1,300 mm in plane and 60 mm in depth. In all 4 slab specimens, 7 steel bars with a length of 1060 mm are distributed along the long side, and 9 steel bars with a length of 1260 mm are distributed along the short side. All the samples were constructed with 8 mm diameter transverse reinforcement bars spaced at 150 mm centers. The concrete cover of all the samples was maintained at 20 mm from the reinforcement bars, as shown in Fig. 5.

2.3 Test setup and procedure

The flexural performance of the samples was assessed via a one-point out-of-plane loading test. The test arrangement is shown in Fig. 6(a). The entire experiment was carried out in a 500 kN self-balancing frame. The reinforced concrete slabs incorporating coal gasification ash were bent via an actuator. Owing to the limited extension length of the actuator, a steel frame made of welded steel tubes was placed under the slab and fixed to the self-balancing frame with four bolts. The frame size is shown in Fig. 6(c). The load was applied downward through a hydraulic jack to bend the slab with a point load. Deflection and cracking patterns were recorded at each load level. The loading was applied under displacement control throughout the entire test.

The vertical displacement measurement points are arranged as follows: three displacement transducers, two of which are installed at the edge of the member plate, are used to measure the displacement warping at the halfway point; one transducer, which is set up at the mid-span position of the floor slab, is used to measure the deflection of the bottom slab mid-span; and the load is applied in the form of a point force to the tested concrete slab, shown as Fig. 6(b).

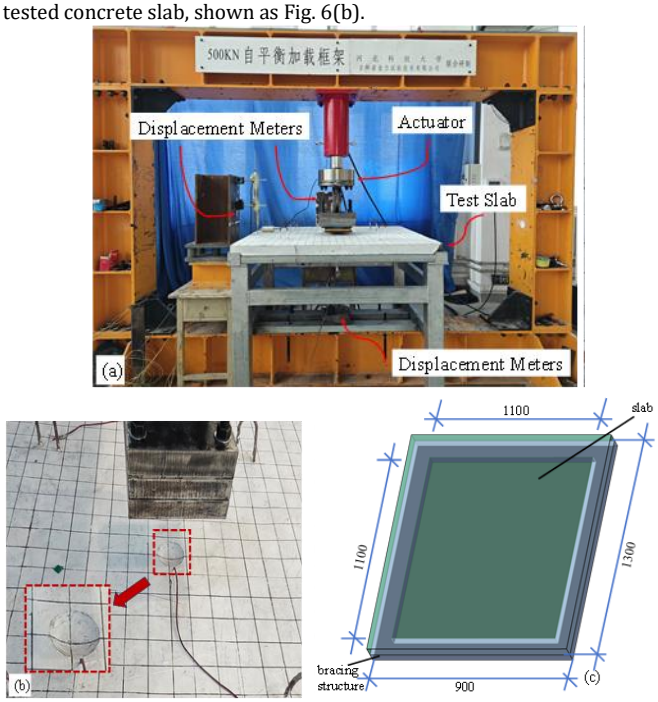

Fig. 6 Test equipment (a) Experimental setup (b) Schematic diagram of the loading point (c) Bracing structure

3. Results and discussion

The static load gradually increased from zero to the maximum load-carrying capacity of the slab, and the deflection of the bottom reinforcement was recorded. For each sample, the maximum deflection and ultimate load capacity were recorded. All the samples exhibited typical bending behavior under bidirectional bending. The slab initially remains elastic until cracking; the sample begins to crack, inelastic deformation occurs, and the bottom reinforcement yields; eventually, the sample fails as the uppermost layer of concrete breaks down.

3.1 Crack extension and damage patterns

Prior to testing, the slabs showed little deformation under self-weight. When the load exceeded about 10 kN, initial cracks appeared at the slab bottom near the loading point, and all specimens cracked at roughly this level. These early cracks did not penetrate the full slab width. With increasing load, crack width and number gradually grew, spreading radially from the center toward the corners in an X-shaped pattern. Maximum crack width exceeded 2 mm. Failure occurred suddenly when bottom concrete was crushed and longitudinal reinforcement yielded, producing similar failure modes across specimens. The number of cracks was about 20 in C30-2, 40 in C40-0, 30 in C40-2, and 20 in C50-2. Notably, slabs with 20% coal gasification slag (CGS) exhibited fewer cracks, confirming enhanced crack resistance.

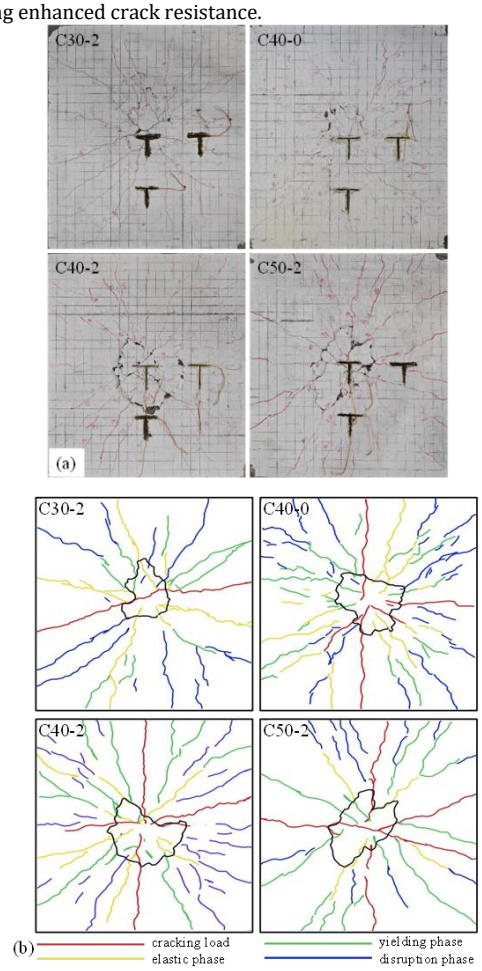

Fig. 7 Crack diagram: (a) Test (b) Fracture diagram

Crack development trends differed with strength grade and mix composition. The crack patterns of each sample at the time of destruction were similar, as shown in Fig. 7(a). The crack patterns on the bottom surfaces of samples C40-0, C40-2, C30-2 and C50-2 are shown in Fig. 7(b), with the red lines showing the cracks appearing under the concrete cracking load, the yellow lines showing the cracks arising from the elastic phase of the concrete, the cracks arising from the concrete being in the yield phase as the green lines, the blue lines showing the cracks appearing under the destructive load, and the black areas showing the broken areas of the concrete. In C30-2, cracks were widely scattered with long paths and rapid propagation, indicating poor crack resistance due to low stiffness. In contrast, C40-2 with CGS showed more controlled cracking: although many cracks formed initially, most remained stable without progressing into the failure stage. This even distribution reflected improved ductility and energy absorption, attributed to the refined microstructure provided by CGS. Compared with C40-2, the plain C40-0 slab displayed fewer but shorter cracks concentrated near the loading path, suggesting limited stress redistribution and lower toughness. The high-strength C50-2 slab showed short, concentrated cracks, but many transitioned quickly into yielding and failure, highlighting its brittle behavior.

Overall, the C40-2 slab achieved the most balanced performance, with CGS delaying severe damage and prolonging the elastic and yielding phases. These results confirm that CGS not only enhances the toughness of medium-strength concrete but also improves crack control and energy dissipation capacity under bidirectional flexural loading.

3.2 Load vs. deflection behavior

The load–deflection curves of slabs incorporating coal gasification slag (CGS) (C30-2, C40-0, C40-2, and C50-2) are shown in Fig. 8. All specimens experienced three stages: elastic, yielding, and failure. In the elastic phase, deflection increased linearly with load, indicating high stiffness and resistance to small deformations. During yielding, the curves flattened, reflecting plastic deformation and declining stiffness. Finally, in the failure stage, stiffness dropped rapidly as the slabs lost load-carrying capacity. Among them, C40-2 showed the best mechanical behavior with a maximum capacity of 31.5 kN, while C30-2 had the lowest at 26 kN. As shown in Table 5, all slabs cracked at 10 kN, and C40-2 sustained significantly higher ultimate loads compared with C40-0, confirming the benefits of 20% CGS addition.

High-strength specimens (C40-2 and C50-2) exhibited greater initial stiffness and maintained good deformation capacity under increasing load. As strength grade increased from C30 to C50, both load capacity and deformation improved. However, C40-2 outperformed others, demonstrating the positive effect of CGS. All slabs cracked at 10 kN, as shown in Table 5, but C40-2 sustained significantly higher ultimate loads compared with C40-0, confirming the benefits of 20% CGS addition.

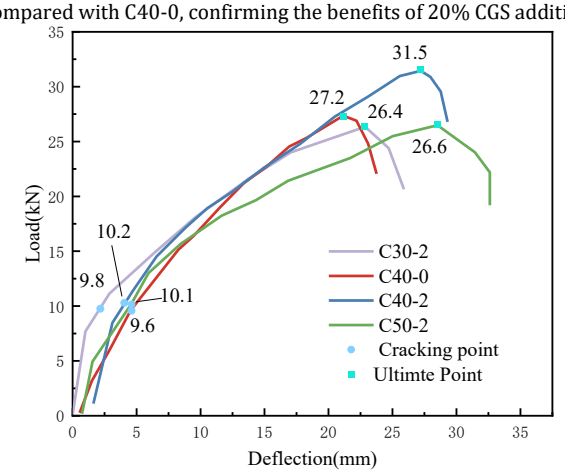

Fig. 8 Load vs. deflection behavior

The enhancement is attributed to the pozzolanic reaction of CGS: silicates and aluminates react with cement hydrates to produce C-S-H gels, which fill pores, densify the matrix, and improve structural strength (Zhao 2024). In C30 concrete, the low matrix strength limited the benefits of CGS, while in C50 concrete, its brittleness and potential microstructural discontinuities reduced ultimate capacity despite higher splitting tensile strength. In contrast, C40 concrete achieved a balance between strength and ductility, with slower crack propagation and improved toughness.

The beneficial effect of CGS is most pronounced in the C40 slabs, which may be explained by the coupling between matrix strength level, crack development characteristics, and the effectiveness of micro-filling/secondary hydration contributions. For the lower-strength C30 concrete, the flexural response is dominated by early cracking and a relatively weak matrix, so the contribution of CGS to matrix densification is not sufficient to fundamentally change the governing failure process at the slab scale. For the higher-strength C50 concrete, the slab tends to exhibit a more brittle response with reduced deformation capacity; meanwhile, the lower water-to-binder ratio and denser matrix may limit the dispersion and reaction efficiency of CGS particles, resulting in a less evident structural-level benefit. In contrast, C40 concrete provides a balanced baseline in terms of strength and deformation capacity, allowing the micro-filling and potential secondary hydration effects of CGS to be more effectively translated into improved crack control, stiffness retention, and overall toughness under bending.

To further quantify the structural toughness, the displacement ductility factor was calculated as $\mu = \Delta u/\Delta y$, where Δy is taken as the deflection corresponding to the cracking point and Δu is the deflection at the ultimate load. The calculated results are summarized in Table 6. The results indicate that the incorporation of CGS improves the deformation capacity of the slabs, particularly for the C40 grade. Although the C50-2 slab also exhibits a relatively high ductility factor, its overall flexural performance is governed by a more brittle response and limited post-peak load retention. In contrast, the C40-2 slab achieves a more favorable balance between load capacity and deformation capacity, resulting in superior structural toughness under bending.

Overall, experimental results confirm that the incorporation of CGS most effectively enhances the performance of medium-strength C40 concrete, improving load capacity, ductility, and durability.

Table 5. Experimental results

Slab ID	Cracking point (Pcr,kN)	Ultimte Point (Pp,kN)
C30-2	9.8	26.4
C40-0	9.6	27.2
C40-2	10.2	31.5
C50-2	10.1	26.6

Table 6. Displacement ductility factor

Slab ID	Δy (mm)	Δu (mm)	μ
C30-2	4.0	22	5.50
C40-0	4.5	21	4.67
C40-2	4.8	25	5.21
C50-2	4.2	24	5.71

4. Finite element simulation

To further elucidate the flexural properties of coal gasification ash concrete slabs and provide a theoretical basis for further research, this section uses the finite element analysis software ABAQUS to simulate and analyze the mechanical properties of concrete slabs mixed with different coal gasification ash contents under concentrated loads, study their structural properties, illustrate the modeling process, and validate the accuracy of the finite element analysis. The purpose of the simulation is to verify the experimental results via numerical methods and to explore the stress distribution, crack development and damage mode of the concrete slab during the stress process in detail to provide complementary and theoretical support for the experimental study.

4.1 Finite element model

The concrete samples were modeled via an ABAQUS. In this work, the concrete damage plasticity (CDP) model was chosen to describe the nonlinear behavior of the material. The CDP model has been thoroughly elaborated in earlier studies (Pawar 2024) in Table 7. The empirical stress–elastic inelastic strain curve of the concrete is determined according to GB50010-2010 combined with Fig. 9(a).

The reinforcement was modeled via ABAQUS. The stress–strain relationship of the reinforcement was modeled via bilinear curves. The rebar is modeled as a nonlinear elastic–plastic material with a modulus of elasticity of 200 GPa, a yield strength of 400 MPa and a Poisson's ratio of 0.3.

In this study, a 3D concrete slab model was created in ABAQUS based on the actual dimensions in the experiment. The dimensions of the model were consistent with those of the experimental samples, and the boundary conditions of four-sided simple support and center loading were used.

Table 7. CDP parameters used in ABAQUS for concrete

Parameter	Dilation Angle (°)	Eccentricity	f_b/f_{c0}	K	Viscosity Parameter
Value	30	0.1	1.16	0.6667	0.0005

Reinforced cement concrete is a composite material, and to obtain realistic test properties, there must be a proper interaction between the reinforcement and the concrete. The reinforcement is represented by line elements, and the other parts are represented by solid elements. The simulations assumed that there is a perfect bond between the reinforcement and the concrete. An embedded technique is used to ensure a perfect bond and no slip between the reinforcement and the concrete. It should be noted that the incorporation of CGS may modify the microstructure of the interfacial transition zone (ITZ) between steel and concrete, which may in turn affect the local bond–slip behavior. In this study, no direct bond–slip tests were performed; therefore, a perfect bond assumption was adopted to focus on the global flexural response of the slabs. This simplification may influence the local interfacial response near cracking regions, but its effect on the global load–deflection behavior and overall failure mode is considered limited, as supported by the good agreement between the experimental and numerical results shown in Fig. 9. When the plate samples were connected to frame supports on the edges, a tangential behavior penalizing friction was set up between the bottom surface of the plate and the frame supports.

In the finite element model, the steel bars are divided into one-dimensional line cells, i.e., T3D2 cells. These line units accurately simulate the mechanical behavior of the steel bars. The concrete slab is meshed via C3D8R 3D solid cells, as shown in Fig. 9 (b). To ensure simulation accuracy, the mesh size is optimized in this paper, and a fine mesh that captures the stress concentration areas is selected.

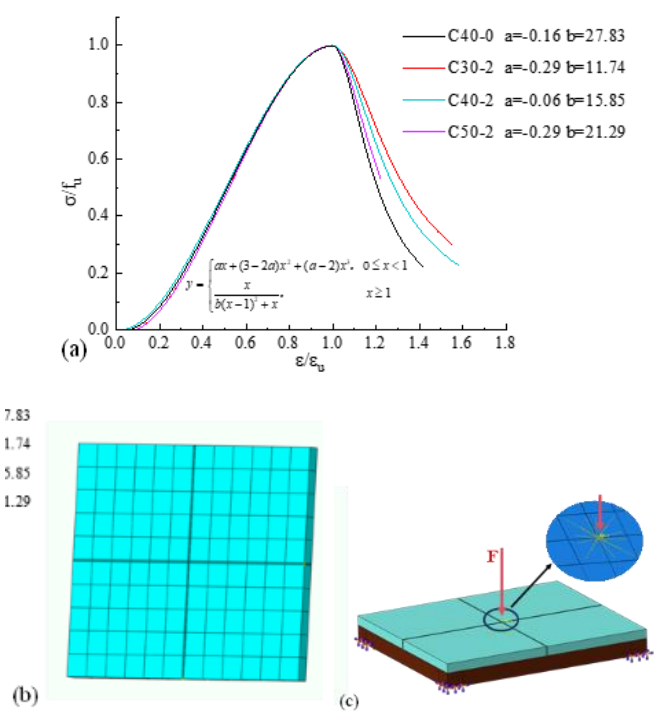

Fig. 9 Simulation modeling process (a) Concrete stress–strain curve (b) Mesh delineation of the plate (c) Schematic representation of the boundary conditions

The boundary conditions of the model were set according to the support method in the experiment, as the four corners of the steel frame were completely and solidly supported, and the friction between the plate and the steel frame was set with a friction coefficient of 0.2. A small square is divided in the center of the plate, and the square is coupled. By defining a boundary condition in the model, a vertical displacement is applied in the middle of the plate, and the applied point of displacement is set at the coupling point, as shown in Fig. 9(c). The multistep loading method is adopted in the loading process, and the load is gradually applied in the displacement control mode. The change relationship between the load and displacement is recorded in real time during the simulation process to gradually approximate the ultimate load applied in the experiment.

4.2 Finite element modeling results

Comparative analysis

The load-deflection curves obtained from both finite element analysis (FEM) and experimental results are presented in Fig. 10. A comparison reveals that the overall trends in the load-deflection curves for the four concrete slabs with different ratios are broadly consistent, confirming the reliability of the finite element model. However, some deviations between simulation and experimental results are observed at specific load and deformation points. These discrepancies may arise from microstructural inhomogeneity within the concrete and the complexity of the actual loading conditions, which could not be fully captured in the simulations. In particular, the finite element model struggles to accurately predict the sudden failure behavior of C30-2 and C50-2 concrete slabs under high loads, likely due to the intrinsic material properties of these concrete mixtures and localized stress concentrations during loading, which the model cannot fully replicate.

Compared with ordinary C40 slab, the peak load of C40 concrete slab with 20 % coal gasification ash increased by 13.1 % and the stiffness increased by 4.3 %. The stress distribution of the ash slag plate is more uniform under the load, and the area of the maximum principal stress concentration area is reduced, indicating that the ash slag alleviates the local stress concentration through the micro-aggregate effect. The load-deflection behavior of the slabs, as observed in both experimental and simulation data, shows consistent trends between the two methods. Although minor deviations are evident at specific loading and deformation points, the general trends—including peak load and failure modes—are in good agreement, further validating the finite element model's effectiveness. These deviations are likely due to the inherent material inhomogeneity and the complexities of the actual loading conditions, which cannot be entirely accounted for in the simulation.

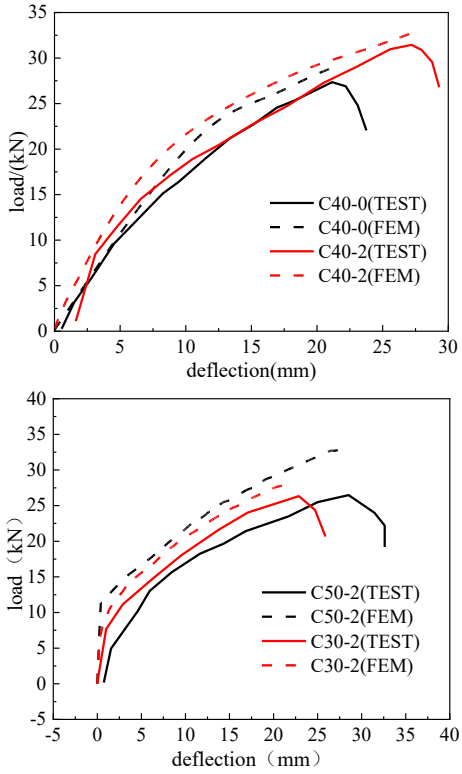

Fig. 10 Load deflection curves

Analysis of C40-2

The displacement cloud diagram is shown in Fig.11 (a). When slab failure occurred, the deformation was mainly concentrated in the central area, which is consistent with the large mid-span deformation observed in the experiment. In the simulation, the warping phenomenon of the four corners gradually appears, and the displacement cloud map is in good agreement with the corner buckling observed in the experiment, which verifies the accuracy of the finite element model to simulate the deformation and displacement distribution of coal gasification slag (CGS) concrete slab. According to the simulation results, the warping height of the four vertex plates is 5.08 mm. This central deformation mode shows that the maximum bending moment of the concrete slab occurs in the central region, resulting in the most significant deformation in the central part. The consistency between the experimental results and the simulation results further verifies the reliability of the simulation method and shows that the finite element model can effectively capture the nonlinear deformation during loading.

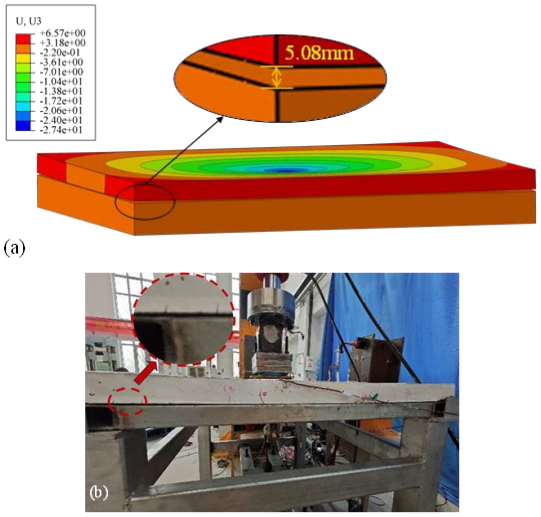

Fig. 11 Three-dimensional figure (a) Displacement cloud map (b) Experimental site with four corners buckled

The displacement cloud of the coal gasification assigned ash concrete slab under the final stress condition is shown in Fig. 12, illustrating the deformation distribution of the slab under loading.

This deformation pattern reflects the typical bidirectional bending behavior of concrete slabs under stress. A symmetrical displacement gradient is observed, with the slab more securely supported around the perimeter, and the central region subjected to concentrated loads, resulting in maximum displacement at the center. This behavior is

consistent with the bending characteristics of concrete slabs under concentrated loading. The incorporation of CGA improves the microstructure of the concrete, enhancing its toughness by filling pores with C-S-H gel generated through the volcanic ash effect, thereby increasing densification and leading to more stable deformation underloading. Concrete slabs with CGA exhibit improved resilience under high-intensity loading, which contributes significantly to structural integrity. By adjusting the amount of CGA, the deformation characteristics of concrete can be optimized, and brittle damage to the slabs can be minimized while maintaining load-bearing capacity.

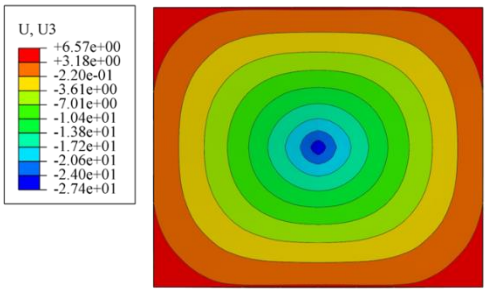

Fig. 12 Deflection contour

Taking C40-2 as an example, Fig.12 shows the evolution process of damage cloud diagram of concrete slab with coal gasification ash. It can be seen from the figure that in the early stage of loading, the damage area is mainly concentrated in the central area of the plate, and when the loading continues, the damage area gradually expands, especially in the four corners of the plate and the middle of the plate. This phenomenon shows that the incorporation of coal gasification as ash improves the overall strength of concrete to a certain extent and slows down the expansion of damage. Although the central area of the plate is still the most stressed part, damage first appears in these areas.

(1) Crack propagation law and damage evolution analysis

As shown in Fig. 13(a–d), the crack propagation in coal gasification slag (CGS) concrete slabs follows a distinct sequence with increasing load. At 0.1F, localized damage first appears at the slab center under the concentrated load, indicating microcrack initiation along the principal stress axis. By 0.3F, damage expands symmetrically in both longitudinal and transverse directions, forming a radial pattern. At 0.5F, cracks extend outward at oblique angles (30°–75°), developing into a complex crack network influenced by stress redistribution and local concentrations at slab corners and edges.

At full load, severe damage regions emerge at the center and extend toward the corners, corresponding well with experimental fracture diagrams and validating the finite element model's accuracy. The incorporation of CGS refines the microstructure, alleviates stress peaks, and improves crack resistance under bidirectional bending. Nevertheless, under high loads, cracks still propagate rapidly at the center and corners, suggesting that while CGS enhances toughness and delays failure, the multidirectional crack growth in high-strength concrete may still compromise long-term durability and structural safety.

By comparing the experimental crack patterns (Fig. 7) and the numerical damage contours in Fig. 13, the influence of CGS dosage on damage evolution of concrete slabs can be further clarified. For the reference slab without CGS (C40-0), damage initiates rapidly at the slab center and propagates along the principal stress paths, resulting in relatively concentrated damage zones and limited stress redistribution.

In contrast, for the slab incorporating 20% CGS at the same strength level (C40-2), the onset of visible damage is delayed, and the damage distribution becomes more uniform over the slab surface. The numerical results indicate that the growth rate of the damaged region is reduced and the extension of dominant cracks is restrained, which is consistent with the experimentally observed denser and more evenly distributed crack patterns. This behavior suggests that the incorporation of CGS promotes stress redistribution and suppresses localized damage accumulation.

For the lower-strength slab (C30-2), although CGS is incorporated, damage propagates rapidly from the central region toward the slab edges, and a wide damage-affected area is formed. This indicates that the relatively low matrix strength limits the effectiveness of CGS in controlling damage evolution. For the higher-strength slab (C50-2), damage remains highly concentrated near the loading region and transitions quickly into a localized failure mode, reflecting a more brittle response.

Overall, the comparative results demonstrate that the effectiveness of CGS dosage on regulating damage evolution is strongly dependent on the concrete strength level. Under the same CGS dosage adopted in this study (20%), the medium-strength slab (C40-2) exhibits the most favorable damage evolution pattern, characterized by delayed damage initiation, reduced damage concentration and more stable propagation, which explains its superior flexural performance observed in both experiments and simulations.

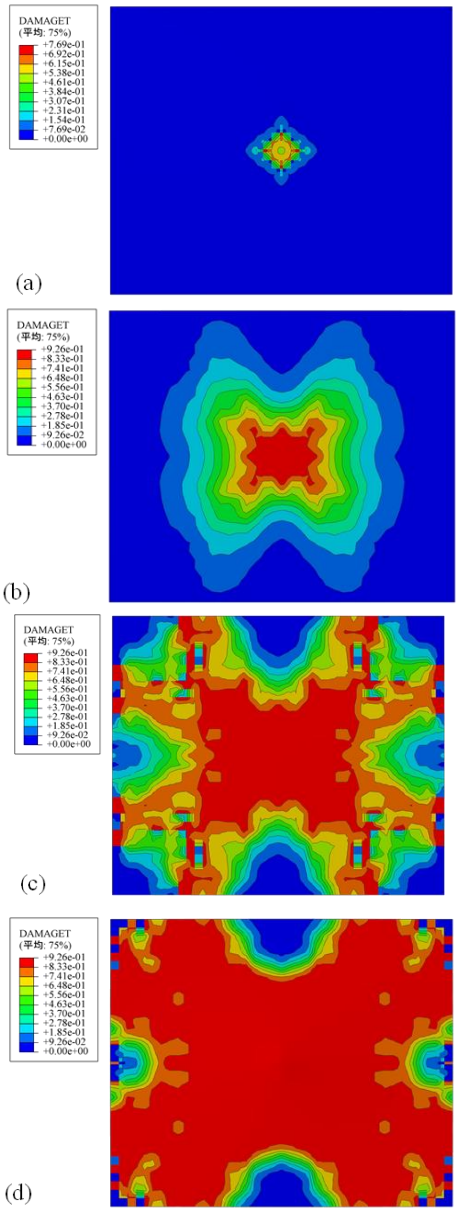

Fig. 13 Change of concrete damage cloud map (a) 0.1F (b) 0.3F (c) 0.5F (d) F

The numerical damage contours further correspond well to the experimentally observed failure modes and crack locations. Both the simulations and experiments show that the dominant damage and cracking initiate at the slab center under the loading point and then propagate along two principal directions toward the slab corners, forming a typical bidirectional flexural failure pattern (Figs. 7 and 13). In addition, the simulated concentration of damage near the mid-span region is consistent with the experimentally observed crushed concrete zone and major crack bands, which further validates the accuracy of the proposed numerical model.

(2) Force Path and Moment Distribution Analysis

Figures 14 and 15 illustrate the force and moment distribution along the slab's long (X) and short (Y) directions. In Fig. 14, the vertical shear force (FZ) peaks near the mid-span, coinciding with the main cracking location observed experimentally and in the damage cloud diagram. The bending moment (MY) and axial force (FX) exhibit smooth, symmetric curves centered at the slab midpoint, confirming that maximum flexural stress occurs there. These stress concentrations correspond to crack initiation and growth, indicating that the slab's structural integrity degrades most rapidly in these critical regions under higher loads.

In Fig. 15, similar patterns appear along the Y direction: FZ peaks at the slab center, while MX follows a parabolic distribution. The horizontal shear force (FY) fluctuates more irregularly near the edges, implying localized stress concentrations and the development of secondary cracks. Together, these results demonstrate that shear and bending effects concentrate at mid-span and that the interaction of longitudinal and transverse stresses produces bidirectional flexural cracking. Overall, the diagrams confirm that CGS-modified slabs display stress redistribution consistent with observed damage and validate the finite element model for predicting failure zones.

The progressive crack propagation in Fig. 11 is supported by the directional force slice diagrams in Fig. 16, which show the distribution of vertical shear force (FZ) across the slab. At the early stage (Fig. 13a), localized damage appears at the center, consistent with a shear peak at the midpoint in Fig. 14(e), indicating that initial cracking is closely linked to vertical shear concentration. With increasing load (Fig. 13b–d), damaged zones expand radially and diagonally, while Fig. 16(a–c) reveals that shear vectors shift from the center toward diagonals and edges, corresponding to the oblique crack paths (30°–75°) observed in simulation.

Slice results in Fig. 16(d–e) also show asymmetrical shear distributions during the transition from center to corners, associated with secondary cracks at slab edges. The close agreement between force path evolution and crack growth confirms the model's accuracy in predicting local failure under bidirectional bending. Overall, Fig. 16 highlights stress redistribution mechanisms, demonstrating that CGS incorporation not only delays crack evolution but also promotes more uniform shear distribution, particularly in medium-strength C40 slabs.

The stress distribution of the steel bar in the concrete slab is shown in Fig.17. From the Mises stress distribution in the figure, it can be seen that the stress concentration of the steel bar mainly appears in the central area of the plate, especially in the area around the loading point. As the load increases, the stress gradually expands around the plate, but the stress value is low, indicating that the steel bar bears less stress in the edge area of the plate. This stress distribution shows that the steel bar plays a major role in the plate, and the main function of the concrete is to bear the compressive stress and help the steel bar transfer the external load. The stress distribution also highlights the interaction between the steel bar and the concrete, indicating that the steel bar plays an effective reinforcing role in the bending process of the concrete slab. With the incorporation of coal gasification ash, the crack resistance of concrete is enhanced, and the stress concentration of steel bar is alleviated, which further improves the performance of concrete slab under high load and reduces local damage and brittle damage.

The overall consistency between the experimental and simulation results confirms that the model is accurate in predicting the performance of CGS-modified concrete slabs under loading conditions. The alignment of experimental and simulation data provides strong evidence for the accuracy of the constitutive model used in this study, offering a reliable tool for further investigations into similar concrete mixtures and bending behaviors under various conditions.

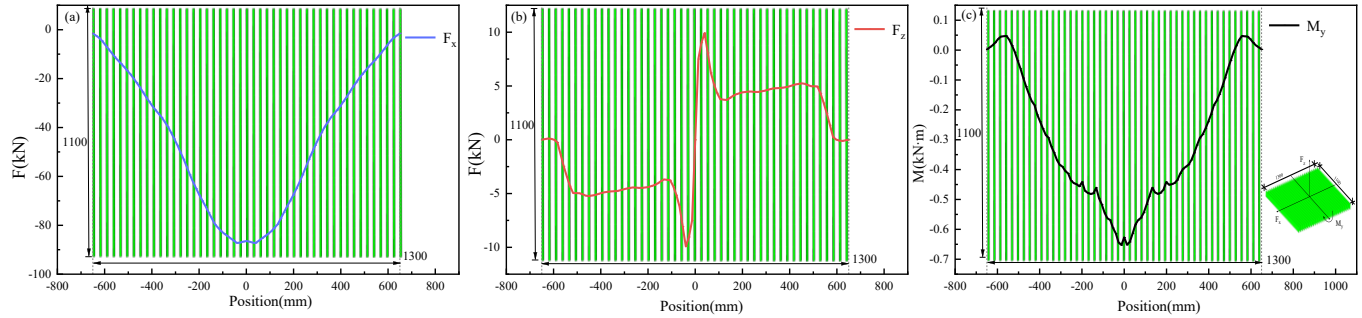

Fig. 14 Long side direction slice by force diagram

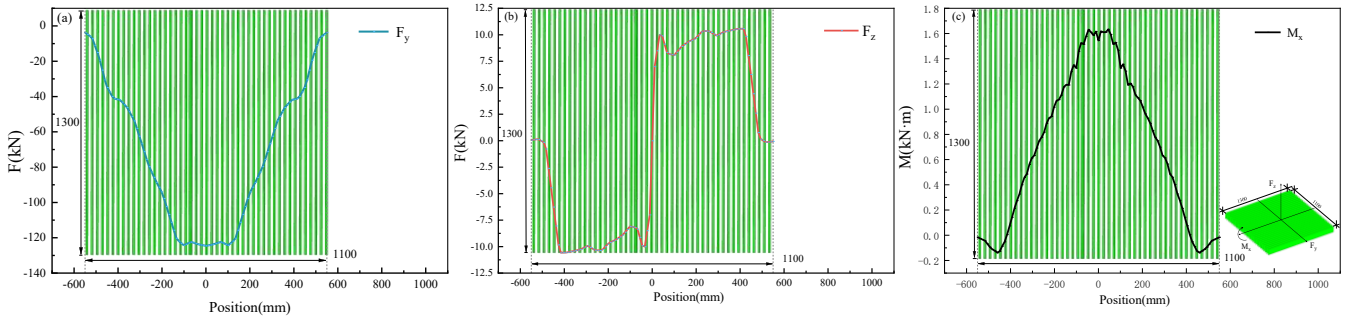

Fig. 15 Short side direction slice stress diagram

(3) Shear force distribution and local failure mechanism

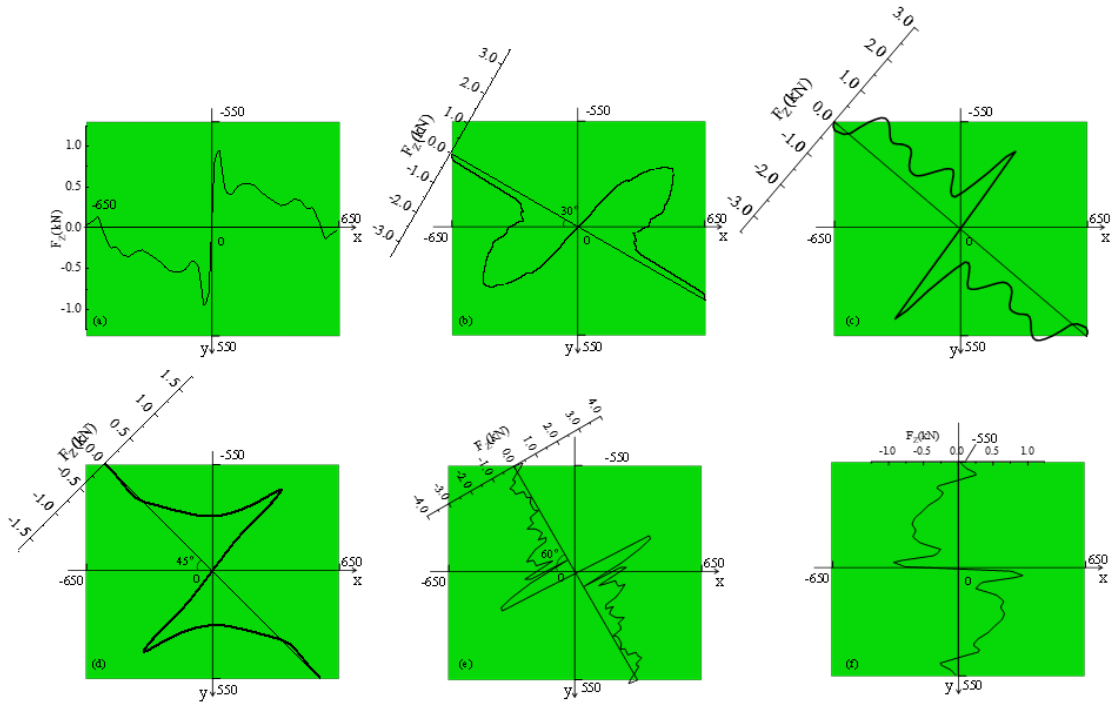

Fig. 16 Slice in different directions

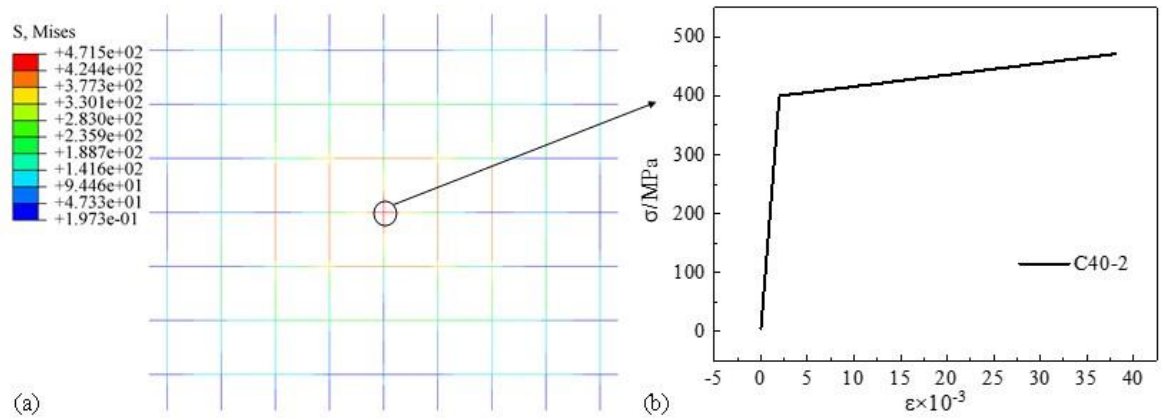

Fig. 17 Steel stress diagram (a) Stress distribution diagram of steel bar (b) Stress-strain diagram of mid-span steel bar

5. Conclusions

This study investigated the flexural behavior of reinforced concrete slabs with different strength grades (C30, C40 and C50) incorporating 20% coal gasification slag (CGS) through experiments and finite element simulations.

(1) The incorporation of 20% CGS improves the flexural performance of concrete slabs, and the improvement is most pronounced for the C40 slab. Compared with the reference slab, the C40 slab with CGS exhibits higher ultimate load and better deformation capacity, which is mainly attributed to the densification of the matrix and the formation of additional C–S–H products induced by the pozzolanic reaction of CGS.

(2) The effectiveness of CGS is strongly dependent on the concrete strength level. For the C30 and C50 slabs, the enhancement in flexural capacity is limited, whereas the medium-strength slab (C40) achieves a more favorable balance between load capacity and ductility.

(3) The proposed finite element model based on the concrete damage plasticity formulation can reasonably reproduce the load–deflection response, failure mode and damage distribution of the tested slabs. The good agreement between the numerical and experimental results confirms that the developed model is suitable for predicting the flexural behavior of CGS-modified concrete slabs.

Future work may consider a wider range of CGS replacement ratios to explore the full potential of CGS in enhancing concrete performance.

Acknowledgements

This research was financially supported by the Hebei Province Natural Science Foundation Project (E2023208080), Hebei Province Postdoctoral Research Funding Project (B2022003024), and Hebei Province Higher Education Institutions Special Research Projects (CXZX2025032).

References

Aineto M, Acosta A, Rincón J M, et al. Production of lightweight aggregates from coal gasification fly ash and slag[J]. World of Coal Ash (WOCA), 2005: 11-15.

ANSYS. A Finite element computer software and user manual for nonlinear structural analysis. Canonsburg, PA.: ANSYS 2007; Inc; 2007.

Fu B, Cheng Z, Wang D, et al. Investigation on the utilization of coal gasification slag in Portland cement: Reaction kinetics and microstructure[J]. Construction and Building Materials,2022, 323: 126587. https://doi.org/10.1016/j.conbuildmat.2022.126587

Guo F, Zhao X, Guo Y, et al. Fractal analysis and pore structure of gasification fine slag and its flotation residual carbon[J]. Colloids and Surfaces A: Physicochemical and Engineering Aspects, 2020, 585: 124148. https://doi.org/10.1016/j.colsurfa.2019.124148

Guo Y, Hu W, Feng G, et al. Study on the excitation effect and mechanism of coal gasification slag based on solid waste[J]. Powder Technology, 2024, 435: 119460. https://doi.org/10.1016/j.powtec.2024.119460

Ishikawa Y. Utilization of coal gasification slag collected from IGCC as fine aggregate for concrete[C]//Proceedings of the EUROCOALASH 2012 conference, thessaloniki, Greece. 2012: 25-27.

Jiang P, Xie C, Luo C, et al. Distribution and modes of occurrence of heavy metals in opposed multi-burner coal-water-slurry gasification plants[J]. Fuel, 2021, 303: 121163. https://doi.org/10.1016/j.fuel.2021.121163

Li Z, Zhang Y, Zhao H, et al. Structure characteristics and composition of hydration products of coal gasification slag mixed cement and lime[J]. Construction and Building Materials, 2019, 213: 265-274. https://doi.org/10.1016/j.conbuildmat.2019.03.163

Luo F, Jiang Y, Wei C. Potential of decarbonized coal gasification residues as the mineral admixture of cement-based material[J]. Construction and Building Materials, 2021, 269: 121259. https://doi.org/10.1016/j.conbuildmat.2020.121259

Matjie R H, Li Z, Ward C R, et al. Chemical composition of glass and crystalline phases in coarse coal gasification ash[J]. Fuel, 2008, 87(6): 857-869. https://doi.org/10.1016/j.fuel.2007.05.050

Pawar A J, Patil Y D, Vesmawala G R, et al. Two-way flexural behavior of biaxial voided slab using cuboidal shape of void formers[C]//Structures. Elsevier, 2024, 62: 106175. https://doi.org/10.1016/j.istruc.2024.106175

Pomykała R. The mechanical properties of coal gasification slag as a component of concrete and binding mixtures[J]. Polish Journal of environmental studies, 2014, 23(4): 1403-1406.

Xiang Y, Jiao Y, Wang L. Effect of sludge amino acid-modified magnetic coal gasification slag on plant growth, metal availability, and soil enzyme activity[J]. Journal of Soil and Water Conservation, 2020, 75(4): 515-526. https://doi.org/10.2489/jswc.2020.00088

Xiang Y, Xiang Y, Gao X. Humic acid coupled with coal gasification slag for enhancing the remediation of Cd-contaminated soil under alternated light/dark cycle[J]. Environmental Science and Pollution Research, 2023, 30(1): 1276-1287. https://doi.org/10.1007/s11356-022-22308-1

Yang P, Liu L, Suo Y, et al. Physical-chemical coupling excitation of low activity coal gasification slag solid waste and its application as a backfill cementitious material[J]. Construction and Building Materials, 2023, 401: 132973. https://doi.org/10.1016/j.conbuildmat.2023.132973

Zeng Q, Liu X, Zhang Z, et al. Synergistic utilization of blast furnace slag with other industrial solid wastes in cement and concrete industry: Synergistic mechanisms, applications, and challenges[J]. Green Energy and Resources, 2023, 1(2): 100012. https://doi.org/10.1016/j.gerr.2023.100012

Zhang L, Yang F, Tao Y. Removal of unburned carbon from fly ash using enhanced gravity separation and the comparison with froth flotation[J]. Fuel, 2020, 259: 116282. https://doi.org/10.1016/j.fuel.2019.116282

Zhang Y, Qu J, Zhang J, et al. Distribution, occurrence, and leachability of typical heavy metals in coal gasification slag[J]. Science of The Total Environment, 2024, 926: 172011. https://doi.org/10.1016/j.scitotenv.2024.172011

Zhang Y, Wang R, Qiu G, et al. Synthesis of porous material from coal gasification fine slag residual carbon and its application in removal of methylene blue[J]. Molecules, 2021, 26(20): 6116. https://doi.org/10.3390/molecules26206116

Zhao Y, Gu X, Xu X. Physical-chemical performance of coal gasification slag with calcination activation utilized as supplementary cementitious material[J]. Construction and Building Materials, 2024, 451: 138776. https://doi.org/10.1016/j.conbuildmat.2024.138776

Disclaimer